

pubs.acs.org/journal/ascecg Research Article

Upgrading Lignocellulose to Porous Graphene Enabled by Deep Eutectic Solvent Pretreatment: Insights into the Role of Lignin and Pseudo-lignin

Hanwen Zhang, Yisheng Sun, Qianwei Li, and Caixia Wan*



Cite This: ACS Sustainable Chem. Eng. 2022, 10, 11501-11511



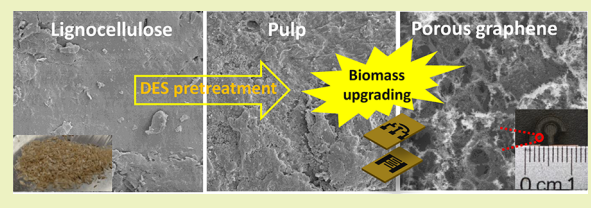
ACCESS I

Metrics & More

Article Recommendations

Supporting Information

ABSTRACT: Converting lignocellulosic biomass into graphene-based materials in a cost-effective approach remains a grand challenge. This study tackled this challenge by implementing direct laser writing (DLW) to lignocellulosic biomass for synthesis of porous graphene (i.e., laser-induced graphene (LIG)). Deep eutectic solvents (DESs), including choline chloride:oxalic acid (ChCl:OA), choline chloride:formic acid (ChCl:FA), and choline chloride:ethylene glycol (ChCl:EG), were used



to enable the fabrication of biomass-based films for DLW. It was found that the cellulose pulp resulting from the ChCl:OA pretreatment was a suitable substrate for LIG formation, requiring no surface treatment of the fabricated film prior to exposure to laser scribing. The obtained LIG had a 3D porous structure and high crystallinity. Pseudo-lignin present in the ChCl:OA pulp was proposed to contribute to the formation of LIG. Lignin in situ regenerated from the pretreatment slurry and redeposited onto the cellulose pulps can further promote the LIG formation on the cellulose pulp film (CPF). The LIG-embedded films were fabricated into on-chip supercapacitors (SCs) and dopamine sensors and further evaluated for electrochemical properties. All the devices showed good energy storage and electrochemical sensing performance, suggesting versatile applications of disposable and low-cost lignocellulose-derived electronics. Overall, the present work demonstrated a feasible and scalable photothermal route based on direct laser writing toward mass production of lignocellulose-derived porous graphene materials.

KEYWORDS: lignocellulosic biomass, lignin, pseudo-lignin, deep eutectic solvents, pretreatment, laser-induced graphene, direct laser writing

■ INTRODUCTION

Advanced carbon materials have been gaining increasing attention in recent years due to their excellent performance in catalysis, sensing, energy, and many other applications. Based on structures and morphology, advanced carbon materials can be categorized into four classes including 0D carbon (e.g., fullerene), 1D carbon (e.g., nanotubes), 3,5 2D carbon (e.g., graphene),6 and 3D carbon (e.g., hierarchical carbon materials). Among these carbon materials, laserinduced graphene (LIG) is considered a new type of 3D porous graphene, which can be produced from a variety of synthetic polymers and natural biopolymers, especially those containing aromatic structures, by direct laser writing (DLW).8 Laser systems like CO₂ and femtosecond lasers can be used to generate localized high temperature and pressure to transform the polymers into few-layer graphene. The single-step laser scribing method does not require tedious wet chemistry or lengthy reactions, making it highly attractive for mass production of graphene-based materials.

Using natural precursors like lignocellulose for graphenebased materials is of great interest to industries and research communities given their renewability, low cost, and abundance. As two of the most abundant natural polymers on earth, cellulose and lignin have been used for LIG production, while lignin appears to be a more structurally favorable precursor due to intrinsic aromatic structures. Large quantities of technical lignin are generated as waste or low-value side streams from pulping and biorefining facilities. Upgrading lignin to valueadded bioproducts is of great importance to the biorefinery industry as it can add revenues to offset the costs for biofuels. It should be noted that technical lignin is often fabricated into a film substrate using a binder (e.g., polyvinyl alcohol (PVA), 10 polyethylene oxide, 11 and cellulose nanofibers 12) for laser writing. For a cellulose-based substrate (e.g., paper or cloth), LIG with good properties was derived and further explored for applications like sensors for detecting strain, humidity, temperature, etc.¹³⁻¹⁵ Xylan, another major component of lignocellulosic biomass, was also explored for LIG-based electronics, which shed light on a new pathway of valorizing lignocellulosic substrates. 16 Surface treatment is often applied to help prevent lignocellulosic materials, especially paper-based substrates, from laser ablation. Recent studies reported LIG

Received: May 4, 2022 Revised: August 5, 2022 Published: August 19, 2022





formation directly from lignocellulosic substrates like cork, wood, and coconut shells without the need for surface treatment given the high thermal stability of substrates and/or optimal lasing conditions such as multiple lasing passes and defocused distance. However, a practical and scalable process has not been developed for converting lignocellulose to LIG given its bulky and heterogeneous nature. To this end, biomass fractionation/pretreatment would be necessary to make it more usable and homogeneous for being readily processed into high-quality LIG. Therefore, research efforts would be much needed to explore viable pathways for mass production of LIG from raw lignocellulosic biomass.

From the perspective of roll-to-roll manufacturing, film substrates are well suited for continuous laser scribing at a large scale. The fabrication of lignocellulose films typically involves pretreatment and film casting, of which pretreatment, such as chemical, physical, and combined methods, is an initial step essentially determining the utility of individual cell wall components. 19-22 The fabrication process should be ensured with reduced complexity and minimized waste generation to achieve cost effectiveness and eco-friendliness. Additionally, lignin extracted during biomass pretreatment should be valorizable to maximize feedstock utilization. Deep eutectic solvents (DESs) comprising a hydrogen bond donor and hydrogen bond acceptor are reported to effectively fractionate biomass for further upgrading into fermentable sugars, nanocellulose, films, etc.²³ For example, DES treatment of cellulose microfibrils can enable extraction of cellulose nanofibers (CNFs) by mechanical defibrillation (e.g., ultrasonication and high-pressure homogenization). 24-26 However, the behavior of lignin during DES pretreatment and further incorporation into a cellulose pulp film still remains unclear. Lack of such understanding can limit the design and selection of DESs for pretreating biomass toward film fabrication. From the point of view of LIG formation, lignin has been reported to play a key role in lignocellulose-based substrates. 12,14,17,18 It should be noted that pseudo-lignin, a lignin-like substance, can be formed from side reactions of sugar degradation compounds (e.g., hydroxymethylfurfural (HMF) and furfural) under severely acidic conditions (Figure S1).²⁷ Pseudo-lignin formation leads to low-quality pulp for enzymatic hydrolysis. Compared to hydrothermal or dilute acid pretreatment, no studies concerning the occurrence of pseudo-lignin formation during DES pretreatment have been reported. Moreover, the effects of pseudo-lignin on the fabrication of biomass-based films have not been studied. It also remains unknown whether and how pseudo-lignin can contribute to porous graphene production, showing a bright side to such a compound rather than being avoided during biomass pretreatment. Therefore, it is important to understand how cellulose-based films incorporating lignin and/or pseudo-lignin evolve into porous graphene under photothermal conditions. For downstream applications of cellulose-based electronic devices, different types of substrates including regenerated cellulose films, 28 cellulose nanofibrils, ²⁹ and paper ³⁰ have been reported. Laser scribing shows great potential in producing cellulose-based electronics as it does not require introducing conductive materials into the cellulose substrates or extra fabrication efforts. 31,32 The development of such electronics also aligns well with green chemistry and eco-manufacturing.

Herein, we proposed to induce porous graphene from lignocellulose-based films and further fabricate it into electronic devices. The work would open a new avenue to

lignocellulose upgrading into graphene-based conductive materials and electronics. Special focus was on understanding the role of lignin and pseudo-lignin formed during biomass pretreatment on both film fabrication and LIG synthesis. Corn stover was used as a model lignocellulosic substrate. The DESs, including choline chloride:ethylene glycol (ChCl:EG), choline chloride:formic acid (ChCl:FA), and choline chloride:oxalic acid (ChCl:OA), were used to fractionate corn stover and compared on their effectiveness in enabling the film-making process for DLW (Figure 1). LIG with good properties was

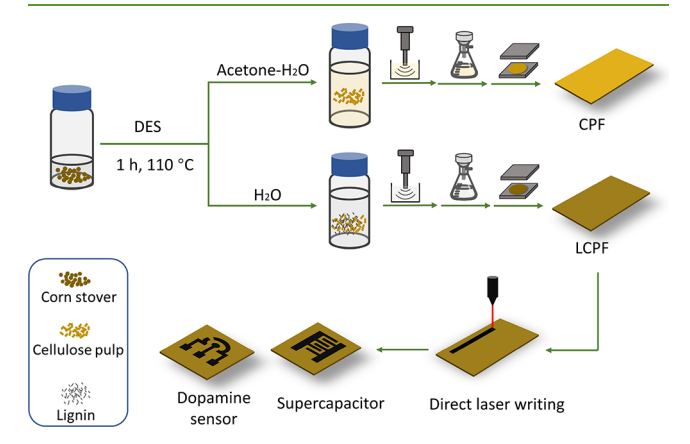


Figure 1. Schematic diagram of fabrication of biomass-based electronics. Corn stover is pretreated by a deep eutectic solvent (DES) followed by addition of an antisolvent (acetone—water mixture or water). The pretreatment slurry is then ultrasonicated and vacuum-filtrated to form wet films. The hot-pressed films are used for direct laser writing to form LIG and further fabricated into on-chip supercapacitors and dopamine sensors.

directly induced on the suitable films under the ambient conditions. Lignin remaining in the pulp or in situ regenerated from the pretreatment liquor was investigated for its role in film fabrication and further LIG formation. Furthermore, pseudo-lignin formed during the biomass pretreatment was found to play a significant role in the formation of graphene. The electronics, including solid-state supercapacitors (SCs) and dopamine sensors fabricated from LIG-embedded films, showed good performance. Thus, this work demonstrated the use of raw lignocellulose enabled by DESs for high-value LIG-based materials toward scalable eco-manufacturing.

■ EXPERIMENTAL SECTION

Materials. Corn stover was collected from the Bradford Farm at the University of Missouri in Columbia, Missouri, USA. The air-dried corn stover was ground and sieved through a 60-mesh screen prior to use. All the chemicals were purchased from Fisher Scientific (Hampton, NH, USA) and used as received.

DES Synthesis and Biomass Pretreatment. The DESs were synthesized by mixing choline chloride (pre-dried at 50 °C overnight) and a hydrogen bond donor (oxalic acid anhydride (OA), formic acid (FA), or ethylene glycol (EG)) at certain molar ratios (i.e., 1:1 for OA and FA and 1:2 for EG) in a glass bottle reactor at 80 °C until a clear liquid was formed. In the case of ChCl:EG, sulfuric acid was added at 1 wt % to the solvent. For pretreatment, the corn stover was mixed with a DES at a mass ratio of 1:15 in a glass bottle reactor and the mixture was then reacted at 110 °C for 1 h in a pre-heated oil bath with continuous stirring (200 rpm). After pretreatment, the glass bottle was cooled down to below 50 °C before further processing.

Fabrication of Biocomposite Films. Acetone—water (50:50, ν/ν) was added to the pretreatment slurry (acetone—water:slurry = 10:1,

v/v). After 10 min of continuous stirring followed by ultrasonication at 20 kHz and 1.2 W/mL for 10 min, the suspension was vacuum-filtered over one piece of Whatman 1PS (silicone treated) phase-separator filter paper. The cellulose pulp (CP) was washed with the acetone—water mixture twice to remove DES and dissolved lignin. The wet CP was placed between two filter papers and pre-pressed at approximately 6 kPa at room temperature for 10 min. The wet CP film was then hot-pressed using a Dabpress hydraulic cylinder hot-press machine (Morgen Innovation Industrial Co. Ltd., Shenzhen, China) at 100 °C and 0.34 MPa for 90 min, obtaining a dried cellulose pulp film (CPF).

To prepare regenerated lignin-incorporated cellulose pulp films (LCPFs), deionized(DI) water was added to the pretreatment slurry (DI water:slurry = $20:1,\ v/v$) as an antisolvent to precipitate lignin from the pretreatment slurry. After continuous stirring for 1 h followed by ultrasonication at 20 kHz and 1.2 W/mL for 10 min, the solids were separated from the liquid over a filter paper via vacuum filtration and washed using DI water twice to remove residual solvent. The dried LCPF was obtained following the procedure for CPFs as described above.

Laser Scribing. A CO₂ laser (VLS 3.50 universal laser system, 10.6 μ m wavelength, 30 W power limit, ~27 in./s maximum scanning speed) was used to scribe the biocomposite films for LIG formation. The image density was set as 5, and the pulse per inch was set as 1000. The laser beam was focused at 4 mm above the irradiated substrate. ¹⁴ The laser scanning speed was fixed at 10% of the upper speed limit. Laser power at 16%, 19%, 22%, and 25% of the upper limit of laser power was used for scribing. All the laser scribing tests were performed under ambient conditions.

Characterization. The compositions of biomass samples were determined following the NREL analytical procedure.³³ Scanning electron microscope (SEM) images were acquired on an FEI Quanta 600 FEG Environmental SEM and a VolumeScope SEM. Nonconductive samples and LIG samples prepared from the bleached pulp film were sputter-coated with 10 nm of platinum before collecting SEM images. Transmission electron microscope (TEM) images of lignocellulosic pulp were acquired on a JEOL JEM 1400 TEM. The sample for TEM imaging was prepared by dropping 5 μ L of the dilute pulp suspension that was dispersed in DI water by the above-described ultrasonication onto a carbon-coated electron microscopy grid. After drying under room temperature for 5 min, a piece of filter paper was used to remove excess liquid on the grid. Subsequently, 5 μ L of 1% phosphotungstic acid (PTA) solution was dropped onto the grid as the negative stain. After ~2 min, the excess liquid was removed by the filter paper. The as-prepared electron microscopy grid was then air-dried at room temperature before imaging. High-resolution transmission electron microscope (HRTEM) images of LIG were taken on a FEI Tecnai F30 G2 Twin TEM. The LIG powders were scraped from the surface of the substrate and sonicated for 5 min in ethanol. The LIG powder suspension (5 μ L) was dropped onto a carbon-coated electron microscopy grid and dried at room temperature before analysis.

Fourier transform infrared (FTIR) spectra were acquired on a Fourier transform infrared spectrometer (Nicolet 4700, Thermo Electron Co., Madison, WI, USA) by 64 scans with a scanning range from 4000 to 400 cm⁻¹. Powder samples were pressed into KBr pellets at a weight ratio of 1:100. The solid-state ¹³C CP/MAS NMR spectra were acquired on a Bruker 400 MHz Avance III wide-bore solid-state NMR operated at 100.64 MHz. Pre-dried powder samples were packed in 7 mm zirconia rotors fitted with Kel-F caps and spun at 7.5 kHz. The analysis was conducted at a 90° proton pulse, 1.5 ms contact pulse, 4 s recycle delay, and 3072 scans.³⁴ Raman spectra were acquired on a Renishaw inVia Raman spectrometer with a wavelength of 633 nm. Tensile testing was conducted on an eXpert 2611 universal testing machine (ADMET Inc., Norwood, MA, USA). The contact angle was measured using a ramé-hart model 200 goniometer (raméhart Instrument, Succasunna, NJ, USA). The sheet resistance (R_s) of LIG was measured using a four-probe bridge resistivity system (Keithley 2400 Series SourceMeter).

X-ray photoelectron spectroscopy (XPS) analysis was carried out on a Thermoscientific Nesxa Photo Electron Spectroscopy system with a monochromatic Al K α X-ray source (at 72 W, 400 μ m diameter slot). XPS survey spectra were obtained with the pass energy at 200 pe and the step size at 0.50 eV. High-resolution spectra were acquired with the pass energy at 50 pe and the step size at 0.10 eV. The spectra were corrected by using the predominate C–C peak as reference (284.4 eV). The deconvolution of high-resolution peaks was performed using XPSpeak 4.1 software. Shirley backgrounds were used for all peak fitting purposes.

Powder X-ray diffraction (XRD) data was collected on a Bruker X8 Prospector diffractometer equipped with an Apex II CCD area detector (Bruker AXS, Madison, WI, USA). LIG powders were scraped from the films under a microscope and loaded directly into polyimide tubes. The powder samples were scanned at 0.02° /step from 20° to 70° .

Fabrication and Analysis of Electronic Devices. LIG was patterned into comb-like interdigitated microelectrodes with 5 mm × 1 mm in $L \times W$ and 1 mm spacing between two neighboring microelectrodes. For the SCs, LIG acted as both an electrode and current collector. Silver paint was applied to the current collector to enhance the electrical connection. Conductive copper tape (3 M) was then attached to the current collector and connected to the electrochemical station. Kapton polyimide tape was used to cover the common area and define the electrode area. A gel electrolyte (1.0 M H₂SO₄/PVA) was then coated onto the microelectrodes and airdried overnight before electrochemical testing. 10 For the dopamine sensor, LIG acted as the working electrode and counter electrode, and a standard Ag/AgCl electrode was used as the reference electrode. The geometrical surface area of the working electrode was \sim 7.1 mm². The analysis of supercapacitors and sensors was performed on an Autolab PGSTAT128N potentiostat (Metrohm). Cyclic voltammetry (CV), galvanostatic charge-discharge (CC), and electrochemical impedance spectroscopy (EIS) measurements were performed to evaluate the performance of SCs. The CV tests were conducted at a scan rate ranging from 0.01 to 0.2 V/s between a potential window of -0.4-0.4 V. The CC tests were conducted at a current density ranging from 0.01 to 0.2 mA/cm². The specific areal capacitances (C_A in mF/cm²) based on the CV curves were calculated by eq 1

$$C_{A} = \frac{1}{2 \times S \times \nu \times (V_{f} - V_{i})} \int_{V_{i}}^{V_{f}} I(V) dV$$
(1)

where S is the total area of LIG electrodes (0.2 cm²), ν is the voltage scan rate (in V/s), V_f and V_i are the potential limits of CV curves, and I(V) is the voltametric current (in mA). $\int_{V_i}^{V_f} I(V) dV$ is the integrated area from CV curves. The specific areal capacitances (C_A in mF/cm²) based on the CC curves were calculated by eq 2

$$C_{\rm A} = \frac{I}{S \times \left(\frac{{\rm d}V}{{\rm d}t}\right)} \tag{2}$$

where I is the discharge current (in mA) and $\mathrm{d}V/\mathrm{d}t$ is the slope of the galvanostatic discharge curve. S is the total area of the LIG electrodes (0.2 cm²). EIS was obtained based on the sinusoidal signal of a 10 mV amplitude at a frequency of 100 kHz to 0.1 Hz.

For CV measurements of the dopamine sensor, the dopamine concentration was 1 mM in phosphate buffer solution (0.1 M PBS, pH = 7) and the scan rate ranged from 10 to 80 mV/s. The dopamine concentration with a range from 1×10^{-6} to 40×10^{-6} M in PBS was used to evaluate the differential pulse voltammetry (DPV).

■ RESULTS AND DISCUSSION

Biomass Compositions and Pseudo-lignin. During the DES pretreatment, hemicellulose and lignin were dissolved by the solvent while cellulose largely remained intact. The compositional analysis showed that the cellulose contents in the pretreated solid/pulp, especially by ChCl:FA and

ChCl:EG, were more than twice that in the untreated corn stover (68.37–65.68% vs 30.55%) because of the substantial removal of non-cellulosic structural components (mainly lignin and xylan) by the pretreatment (Figure 2a,b). The xylan

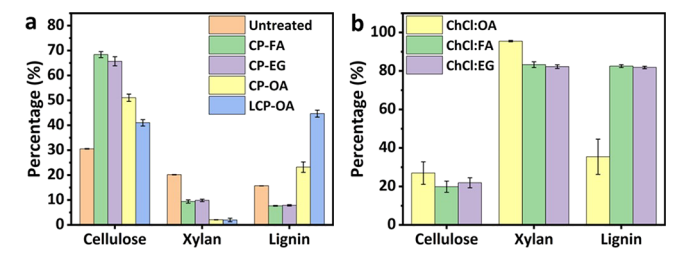


Figure 2. (a) Compositions of untreated corn stover, cellulose pulp (CP), and regenerated lignin-containing cellulose pulp (LCP) resulting from the pretreatment by three DESs. (b) Component removal by three DESs.

content of the cellulose pulp resulting from ChCl:OA pretreatment (CP-OA) was minor (2.09%), which was much lower than the other two (9.42% for CP-FA and 9.88% for CP-EG), indicating that ChCl:OA promoted more hemicellulose hydrolysis under the same conditions. On the other hand, the lignin content in CP-OA was much higher than in the other two pulps (23.21% vs 7.68-7.87%), which should be partially attributed to the pseudo-lignin formation during the ChCl:OA pretreatment.³⁵ This phenomenon was also reflected by the dark color of CP-OA. In contrast, the other two pulps (CP-FA and CP-EG) showed a grayish color and the untreated corn stover showed a yellowish color (Figure S2a). Pseudo-lignin is reported to have a lignin-like structure formed from sugar degradation products as a result of severe biomass pretreatment under acidic conditions.³⁶ However, the compositional analysis cannot distinguish pseudo-lignin and genuine lignin. SEM images reveal that, after pretreatment, the particles with irregular shapes were formed on CP-OA (Figure 3b-d and S2b), which is similar to pseudo-lignin previously reported,³ while the untreated corn stover, CP-EG, and CP-FA showed smooth surfaces (Figure 3a and Figure S2c,d). At higher magnification (Figure 3d), pseudo-lignin particles showed aggregates of smaller particles (~70 nm).

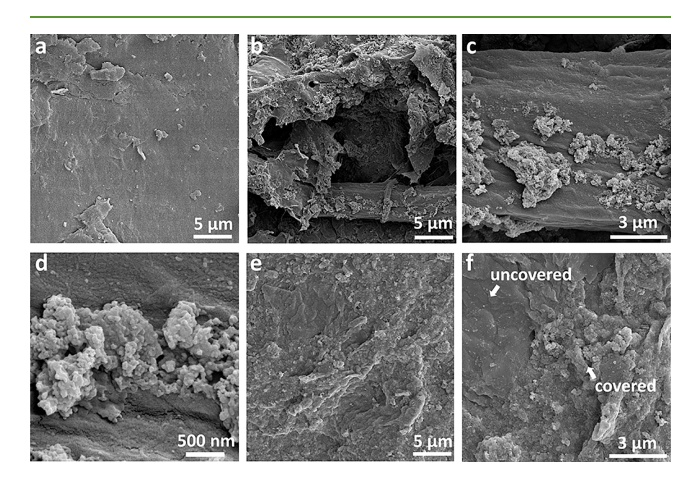


Figure 3. SEM images of untreated biomass and pulp. (a) Untreated corn stover. (b-d) Cellulose pulp resulting from ChCl:OA pretreatment (CP-OA). (e, f) Regenerated lignin-containing cellulose pulp (LCP-OA).

The formation of pseudo-lignin was confirmed by using the bleached/delignified pulp from corn stover and model compounds with the methods detailed in Supporting Information. As shown in Figure S3a,c, the bleached pulp contained 74.20% holocellulose (including cellulose and xylan) and showed a whitish color because of near-complete delignification (91.8% lignin removal). The ChCl:OA-treated bleached pulp (BP-OA) showed a dark color similar to that of the ChCl:OA-pretreated corn stover (Figure S3b). The compositional analysis also revealed that the pretreatment led to an almost 10-fold increase in lignin content of the bleached pulp (2.07% lignin before vs 20.33% lignin after) (Figure S3c). Such a change clearly indicated the formation of pseudo-lignin. 13C NMR spectra of BP and BP-OA are compared in Figure S4a. Strong signals between 108.9 and 57.6 ppm are the characteristic peaks from both cellulose and hemicellulose. Two peaks at 20.8 and 174.0 ppm disappeared after the pretreatment, which are assigned to the carbon of CH₃ and C=O in the acetyl group of hemicellulose.³⁸ This indicates the cleavage and degradation of O-acetyl in hemicellulose during ChCl:OA pretreatment.³⁹ On the other hand, a sharp peak at 54.4 ppm is associated with the carbon in methoxy groups related to aromatic structures.27 The appearance of this peak suggested the formation of pseudolignin with aromatic structures resulting from condensation reactions of sugar degradation products.³⁷ Intensified signals at 10-55 ppm assigned to aliphatic carbon, 120-160 ppm assigned to unsaturated carbon, and 197-215 ppm assigned to carbon in unconjugated C=O were observed in BP-OA. 27,37 These NMR results indicated that the pseudo-lignin, which has both aromatic structures and aliphatic chains with methoxy and carbonyl groups, was formed in BP-OA. To rule out the influence of genuine lignin, a mixture of pure glucose and xylose, representing two key intermediates resulting from holocellulose hydrolysis during the DES pretreatment, was pretreated under the same conditions to further confirm the formation of pseudo-lignin. The characteristic peaks that indicate the formation of aromatic structures from these model compounds were well identified in the FTIR spectrum (Figure S4b). Absorbance peaks at 1462, 1512, and 1618 cm⁻¹ were observed, which were all assigned to C=C stretching in aromatic rings. ^{27,35,40} The two peaks at 1021 and 1163 were of C-O stretching associated with HMF, furfural, carboxylic acids, and alcohols.²⁷ The peak at \sim 1700 cm⁻¹ arose from C= O stretching in carboxylic acids, conjugated aldehydes, or ketones.²⁷ FTIR data suggested that various small compounds derived from lignocellulose can be further condensed into humin-like macromolecules including pseudo-lignin.

TEM images of BP-OA after ultrasonication are shown in Figure S4c,d. Micro-/nanofibrils were clearly observed, which confirmed ultrasound-assisted defibrillation. Nanospheres were also observed with the majority most likely originating from pseudo-lignin, which agreed with prior studies. The pseudo-lignin formation was also evidenced by the morphological change of BP-OA (Figure S5). The bleached pulp initially had a smooth surface and then showed small pseudo-lignin aggregates on the surface when the ChCl:OA pretreatment was applied. Like CP-OA, most of xylan was hydrolyzed and further degraded, primarily contributing to the pseudo-lignin formation. In contrast, both ChCl:FA and ChCl:EG pretreatments led to less xylan removal (82.23–83.28 vs 95.48% by ChCl:OA) under the same conditions (Figure 2b), which did not lead to pseudo-lignin formation. As shown in

SEM images, the CP-FA and CP-EG showed no pseudo-lignin aggregates on the pulp surfaces (Figure S2c,d). Thus, 7.67—7.87% residual lignin remaining in these two DES pulps should be genuine lignin. The findings also provided insights into the fates of carbohydrate degradation products during the pretreatment using different DESs.

Lignin in situ regenerated from the pretreatment slurry was also studied for its redeposition onto cellulose pulp. It was found that the surface of regenerated lignin-containing cellulose pulp (LCP-OA) was covered primarily with the mixture of regenerated lignin and pseudo-lignin (Figure 3e,f). The lignin content in the pulp increased from 23.21% to 44.68% indicating the incorporation of regenerated lignin (Figure 2a). From the perspective of fermentable sugar production, the presence of lignin and/or pseudo-lignin in a pulp can negatively affect the enzymatic hydrolysis efficiency of the cellulose pulp because cellulose accessibility and/or cellulase activities can be reduced by non-productive binding to enzymes.³⁵ Nevertheless, this work showed that both types of lignin were good precursors for LIG formation.

Biocomposite Films. Biocomposite films were fabricated directly from the cellulose pulp only (CP) or that redeposited with in situ regenerated lignin (LCP), as illustrated in Figure 1. As discussed above, the cellulose pulp only should be free of dissolved carbohydrates and regenerated lignin as well as other soluble impurities. It was first facilely defibrillated to micro-/ nanofibrils via ultrasonication, and the subsequent hot press can promote the interaction of cellulose and residual lignin in the pulp as well as self-bonding of lignin. In the case of LCPF fabrication, water was added as an antisolvent to the pretreatment slurry to regenerate/precipitate out lignin as aforementioned.¹⁹ The regenerated lignin was redeposited onto the cellulose pulp, which in turn was used for the fabrication of biocomposite films. The morphologies and microstructures of the corn stover-based CPF and LCPF were characterized by SEM. Both substrates showed a dense and relatively smooth surface (Figure 4a,c). At higher magnifica-

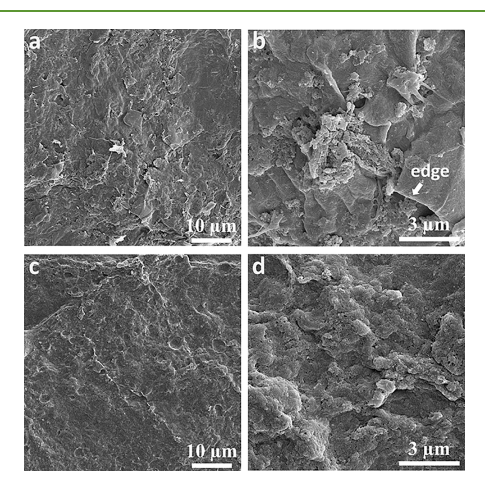


Figure 4. SEM images of films. (a, b) CPF. (c, d) LCPF.

tion, laminated edges can be found on the CPF due to the layered cellulose fibrils (Figure 4b). Pseudo-lignin still covered part of the cellulose surface. However, on the LCPF, no laminated edges of cellulose were observed. Most of the cellulose surface was covered with pseudo-lignin and/or regenerated lignin (Figure 4d). Despite the film composition, pseudo-lignin and regenerated lignin seemed to not fully melt

upon hot press even though a temperature of over 100 °C was also tested. On the other hand, it suggested that pseudo-lignin and regenerated lignin would have a relatively high glass transition temperature (T_g) . A poor interfacial interaction of cellulose and lignin/pseudo-lignin should largely contribute to the low tensile strength of the biocomposite films (Figure S6a,b), similar to that of some other natural polymer-based films such as polyhydroxyalkanoates⁴² and Eucommia ulmoides gum. 43 Nevertheless, the tensile strength of the LCPF was 63% higher than that of CPF (Figure S6b) because of mechanical reinforcement by the regenerated lignin that acted as an adhesive for binding cellulose fibrils. 19,44 Both films had good waterproof properties as evidenced by high contact angles (i.e., 89.8° for the CPF and 79.4° for the LCPF) (Figure S6c), which was attributed to the hydrophobic nature of lignin/ pseudo-lignin. It is worth mentioning that the cellulose pulp resulting from the other two DESs (CP-FA and CP-EG) can also be readily fabricated into CPFs via ultrasonication (Figure S7b,c). Moreover, the same technique based on DES pretreatment for biocomposite film fabrication can also be applied to other biomass feedstocks such as aspen wood and hemp hurd (data not shown). Since this work was focused on corn stover as a model substrate for biocomposite films and subsequent LIG formation, we did not further explore other films. Therefore, our future work on the direction of DES pulp for biocomposite films would aim to further investigate the impact of lignin (pseudo vs genuine) and other biomass feedstocks on film properties and downstream applications.

LIG Characteristics. The CPFs resulting from three DES pretreatments were tested for LIG formation with no surface treatment. Interestingly, the CPF-OA showed LIG formation, while the CPF-EG and CPF-FA were burned out during the laser scribing (Figure S7). The difference should be attributed to the presence of pseudo-lignin on the surface of CPF-OA. On the other hand, although both CP-EG and CP-FA had residual lignin (5-6%) (Figure 2a), the lignin contents were not high enough to make the respective films inducible for porous graphene by laser scribing. In contrast, the pseudolignin with high thermal stability and repetitive aromatic units allowed the lignocellulose-based biocomposite films to directly suit DLW for porous graphene synthesis without additional treatment. In general, fire retardant treatment and controlling the lasing atmosphere would have to be applied to prevent burning or ablating the substrates when the laser is directly applied onto cellulose-based materials such as filter paper and cloth. 14,17 The successful induction of the conductive layer from the CPF-OA without those requirements suggested that tailoring the surface chemistry of biomass like incorporating pseudo-lignin can favor graphitization of biomass-derived compounds upon laser treatment. In the latter sections, we focused on CPF-OA and LCPF-OA for LIG formation to understand the role of pseudo-lignin versus regenerated lignin.

Different laser power levels were applied to generate LIG on both CPF-OA and LCPF-OA. The LIG generated on CPF-OA and LCPF-OA is denoted as CPF-LIG and LCPF-LIG, respectively, with the numbers as suffix indicating the laser power levels applied. Figure 5a shows the Raman spectra of LIG from the CPF at four laser power levels. The Raman spectra show three prominent peaks: the D peak at ~1335 cm⁻¹ associated with defects, the G peak at ~1581 cm⁻¹ originating from in-plane vibrations of sp²-bonded carbon atoms, and a 2D peak at ~2667 cm⁻¹ originating from the second-order zone-boundary phonons. When the laser power

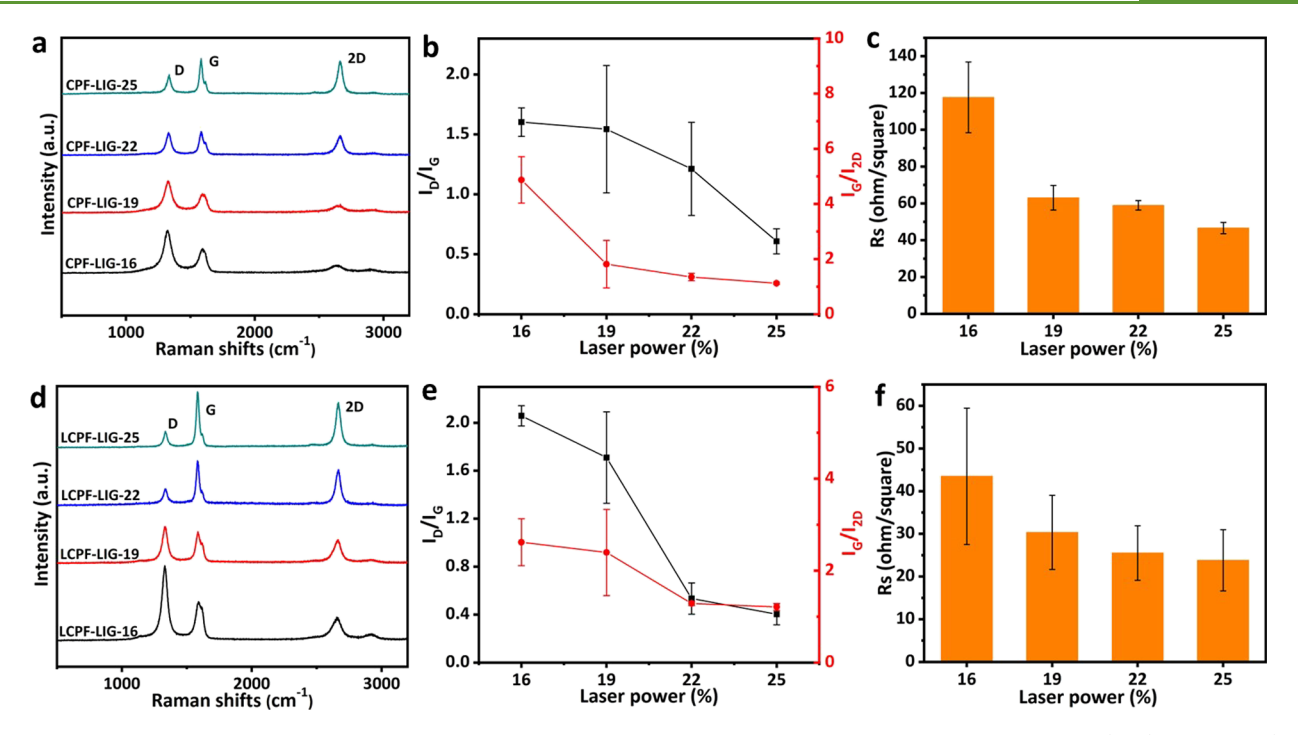


Figure 5. Raman spectra, I_D/I_G , and I_G/I_{2D} ratios, and sheet resistance of LIG obtained at different laser power levels. (a–c) CPF-LIG. (d–f) LCPF-LIG.

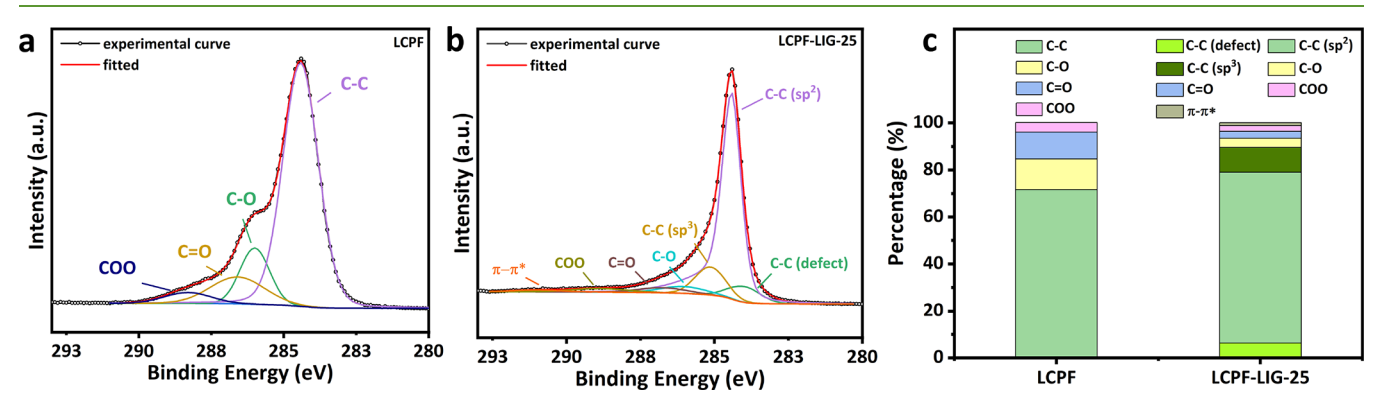
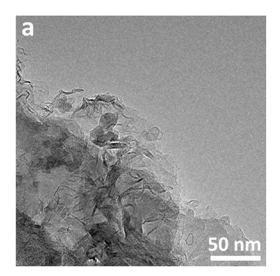


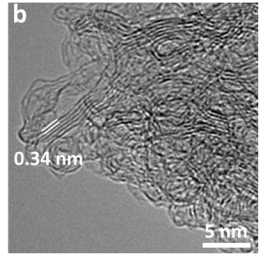
Figure 6. Deconvoluted C 1s XPS spectra of films and LIG: (a) LCPF and (b) LCPF-LIG-25. (c) Distribution of carbon chemical states.

was low (16% and 19%), a weak 2D peak and a strong D peak were observed, indicating the formation of low-graphitic carbon with high defects. The increase in laser power from 19% to 25% led to higher quality LIG as reflected by the increased intensity of the 2D peak and the decreased intensity of the D peak. The intensity ratios of D and G peaks (i.e., I_D / I_G) were used to evaluate the defect density in LIG.⁴⁶ When 25% laser power was used, the lowest I_D/I_G ratio (0.61) was observed (Figure 5b), which demonstrated the lowest density of defect. The crystallite size (L_a) along the α axis was 57.3 nm as calculated based on eq S1, which was the largest among the power levels applied.⁴⁷ Moreover, the smallest I_G/I_{2D} ratio (1.12) of the CPF-based LIG obtained at 25% power also indicated that the fewest number of graphene layers was formed (Figure 5b). Like the CPF, the laser power at the two lower levels (16% and 19%) was inadequate to well induce LIG on the LCPF (Figure 5d). However, when a higher laser power was applied, the LCPF appeared to be more inducible for highquality LIG as evidenced by the substantially reduced I_D/I_G ratios compared to the CPF (Figure 5e). In addition, the 2D peak of LCPF-LIG-25 showed high symmetry, which can be

fitted with only one Lorentzian peak. This 2D band profile is consistent with other few-layer graphene materials.⁴⁵ These findings suggested that the lignin regenerated and redeposited onto the surface of cellulose fibers can serve as a more effective precursor for higher-quality LIG when sufficient laser power is applied to lignocellulose-based films.

The LIG induced from both the CPF and LCPF resulting from ChCl:OA was highly conductive, as evidenced by a low R_s (Figure 5c,f). With the increase of laser power from 16% to 25%, the R_s of CPF-LIG decreased from 118 to 47 Ω /square. This corroborated that a higher laser power led to a higher degree of graphitization, resulting in better conductivity. The LCPF-LIG had a lower R_s than the CPF-LIG at a given laser power level due to the presence of extra amounts of lignin in the substrate. The well-distributed lignin can help form the 3D hierarchical graphene with better internal connection, which leads to better conductivity. The lowest R_s (24 Ω /square) was observed on the LCPF at 25% laser power, which is comparable to the LIG formed on commercially available substrates (i.e., polyimide and poly(ether imide) 48).





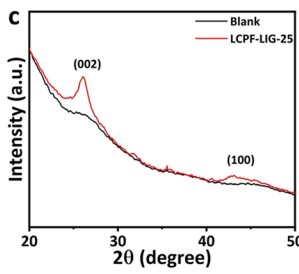


Figure 7. LCPF-LIG-25 electrode. (a) TEM image. (b) HRTEM image. (c) XRD.

The surface chemistry of the LCPF and LCPF-LIG-25 was studied by XPS. The XPS survey scan was first used to study the surface elemental composition, and the acquired survey spectra are depicted in Figure S8. The LCPF was rich in C and O, which was expected from the cellulose and lignin/pseudolignin.³⁹ LCPF-LIG-25 also showed the presence of C and O as two major elements due to oxygen-containing functional groups. Other minor components including Si, N, and Al should originate from the feedstock (i.e., corn stover) and possible impurities introduced during the film fabrication as described above. 49 High-resolution C 1s XPS spectra of the LCPF and LCPF-LIG-25 are compared in Figure 6a,b with the chemical state distribution of C 1s depicted in Figure 6c. Before laser scribing, the C 1s XPS spectra can be fitted into four symmetric peaks: C-C at 284.4 eV, C-O at 286.0 eV, C=O at 286.6 eV, and C-O=O at 288.3 eV. 50 Significant amounts of C/O linkages existing on the surface of the LCPF can be attributed to oxygen-containing functional groups and interlinkages (e.g., -OH, C-O-C, -COOH) in cellulose and lignin/pseudo-lignin. After laser scribing, the C 1s XPS spectra of LCPF-LIG-25 can be fitted into one prominent asymmetric C-C (sp²) peak at 284.4 eV and six symmetric peaks: C-C with vacancy defects at 284.0 eV, C-C (sp³) at 285.1 eV, C-O at 286.0 eV, C=O at 286.8 eV, C-O=O at 288.9 eV, and π - π * shake-up at 291.0 eV.⁵¹⁻⁵³ The asymmetric C-C peak fittings are often used for the primary C-C peak in graphitic carbons due to the semi-metal effects resulting from conduction band electrons.⁵⁴ Two additional C-C peaks at 284.0 and 285.1 eV indicated that minor amounts of defects and amorphous carbon existed in the LIG, which agreed with the Raman results. The significant increase of the total C-C bond percentage (from 71.7% in the LCPF to 89.6% in LCPF-LIG-25) confirms the graphitization of LCPF during the laser scribing. Several minor C/O linkages existed in LCPF-LIG-25, which suggested the oxidization of LIG. However, the total contents of C/O linkages in LCPF-LIG-25 were lower than that in LCPF because of the cleavage of C-O/C=O bonds occurring during the laser scribing.

A film was also fabricated from the bleached pulp resulting from ChCl:OA treatment (BPF-OA) and used to further investigate the role of pseudo-lignin in LIG formation. As shown in Figure S9a-c, a porous graphene structure was formed on the film when 25% laser power was applied. The Raman spectrum indicated the formation of LIG with lower defect ($I_{\rm D}/I_{\rm G}=0.32$) than that derived from the LCPF (Figure S9d). It was evident that pseudo-lignin is a good precursor for high-quality LIG in addition to a surface modification agent of cellulose fibers for preventing laser ablation. Like genuine lignin, pseudo-lignin can also yield LIG with tailored LIG characteristics with desired attributes. This depends on the type of substrate used for film fabrication (e.g., DES-

(pre)treated corn stover or bleached pulp) and laser conditions. On the other hand, the fact that pseudo-lignin is a precursor of LIG points to a direction for using holocellulose or carbohydrates as a new source for porous graphene.

The LIG formed on the LCPF at a 25% laser power level was used for further characterization to confirm the formation of the few-layer graphene structure. TEM was used to study the micro-/nanostructures. Figure 7a shows the highly wrinkled structure at the edge of LIG flakes. These structures have been shown to improve the performance of carbon-based energy storage devices as better ion diffusion can be facilitated. 55-57 The HRTEM image in Figure 7b shows the long graphene layers stacking together. The lattice space is around 0.34 nm, which is consistent with other few-layer graphene materials. 10,58,59 XRD was used to study the crystalline structure of graphene (Figure 7c). The LIG shows two peaks at $\sim 26.1^{\circ}$ and $\sim 43.1^{\circ}$, corresponding to the (002) and (001) plane of the graphene layer, respectively. The (002) peak suggests an interlayer spacing of 0.34 nm (Bragg's law), which agreed with the result from HRTEM. The tailed (002) peak suggested that some amorphous carbon would exist in the

Porous LIG structures were clearly observed with the LIG formed on both CPF and LCPF at 25% laser power (Figure 8).

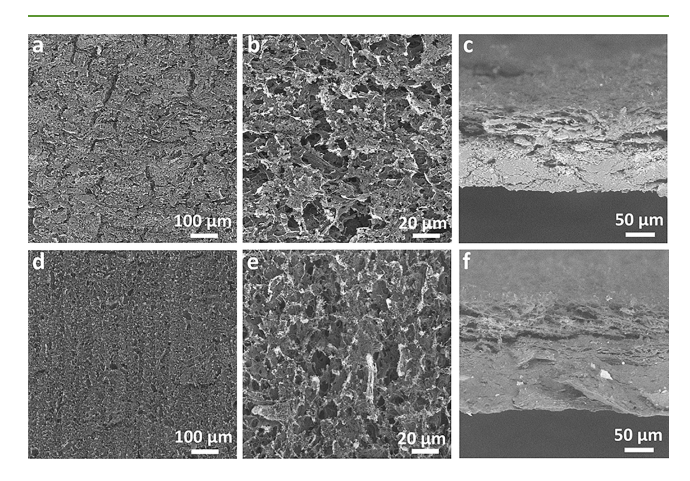


Figure 8. SEM images of LIG. (a-c) CPF-LIG-25. (d-f) LCPF-LIG-25.

A porous LIG structure was formed on both film substrates due to the release of volatile components such as CO₂ and H₂. More cracks and larger pores were observed from the LIG derived from the CPF than from the LCPF. This would be due to the higher cellulose content in the CPF, which could contribute to the formation of more gaseous components during lasing and subsequently destroy the continuity of the LIG film. The large gaps in the LIG can also affect the

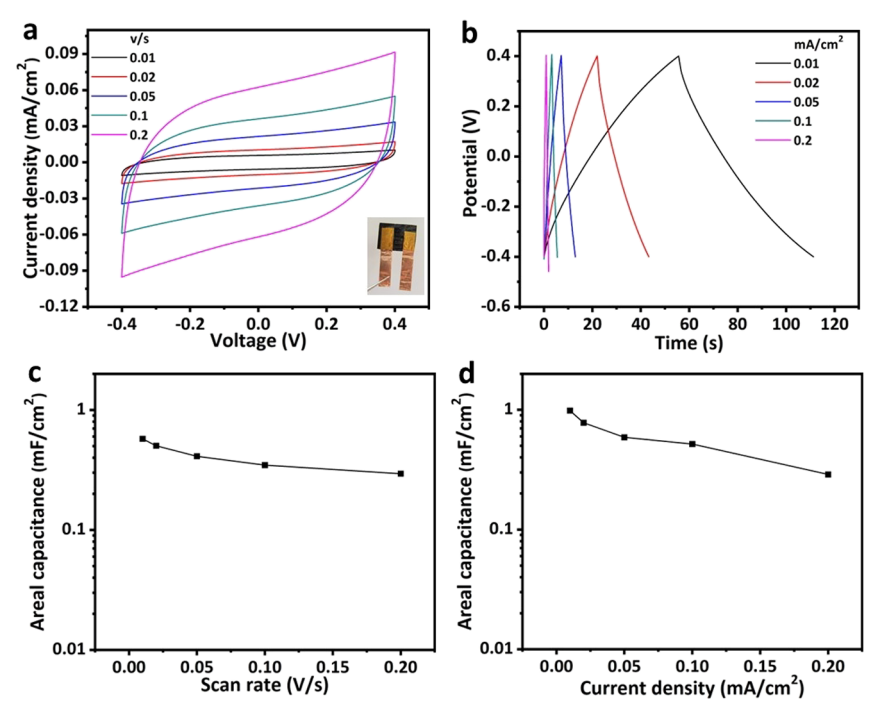


Figure 9. Performance of SCs fabricated from the LCPF-LIG-25 electrode. (a) CV curves. (b) CC curves. (c) Specific areal capacitance (C_A) calculated from CV curves as a function of the scan rate. (d) Specific areal capacitance (C_A) calculated from CC curves as a function of the current density.

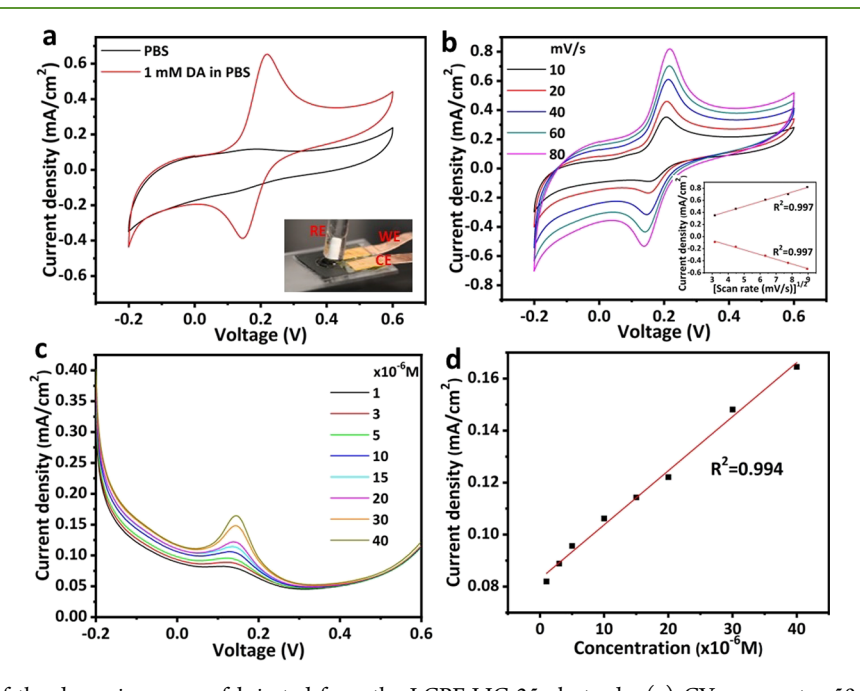


Figure 10. Performance of the dopamine sensor fabricated from the LCPF-LIG-25 electrode. (a) CV curves at a 50 mV/s scan rate in 1 mM dopamine solution. Inset: testing set-up (RE: Ag/AgCl (3 M KCl) reference electrode; WE: working electrode; and CE: counter electrode). (b) CV curves at different scan rates in 1 mM dopamine solution. Inset: relationship between the peak redox current density and scan rates. (c) DPV curves at different concentrations of dopamine. (d) Relationship of the oxidation peak current density from DPV and concentration of dopamine. Linear fitting is used to determine the sensitivity of the electrode.

electrical conductivity of LIG, resulting in a higher R_s for the CPF-LIG. Cross-sectional SEM images show a relatively obvious boundary between the porous LIG structure and the film substrates (Figure 8c,f). The bottom sides of the films were not affected by the laser power, which can provide support for further on-chip electronic applications.

Electrochemical Performance. Supercapacitors. The on-chip solid-state SCs were fabricated from the LIG-embedded biomass-based films without LIG transfer. In particular, the LCPF resulting from ChCl:OA pretreatment discussed above was laser-scribed at a 25% power level and used for prototyping. The highly conductive LCPF-LIG-25 in situ embedded onto the LCPF and worked as both a current

collector and active electrode, while the LCPF itself served as a suitable substrate for the SCs. Figure 9 shows the performance of on-chip SCs fabricated from LCPF-LIG-25. All the CV curves had good pseudo-rectangular shapes (Figure 9a), indicating an electrical double-layer capacitive (EDLC) behavior. The high conductivity of the electrodes made from LCPF-LIG-25 allows electrons to move quickly within the electrodes to form the electrical double layer even when the scan rate was high. The CC curves at different current densities are plotted in Figure 9b. The nearly triangular shape of CC curves at all the current densities confirms the good capacitive behavior. Specific areal capacitances (C_A) calculated from CV and CC curves are plotted in Figure 9c,d, respectively. The highest C_A from CV curves is 0.57 mF/cm² at a scan rate of 0.01 V/s, and that from CC curves is 0.98 mF/cm² at a current density of 0.01 mA/cm². Such capacitance can be further improved by functionalizing the precursor through heteroatom doping or introducing pseudocapacitive/conductive materials to LIG. 10,60 The CV curves and CC curves of the SC fabricated from CPF-LIG-25 are plotted in Figure S10a,b. The decent capacitance of CA calculated by the CV and CC curves in Figure S10c,d indicates that both the LCPF and CPF embedded with LIG-25 can serve as good substrates for electronic devices.

The equivalent series resistance (ESR) of SCs fabricated from CPF-LIG-25 and LCPF-LIG-25 were 205 and 57 Ω , respectively (Figure S11). The lower ESR of the SC fabricated from LCPF-LIG-25 can be attributed to the excellent conductivity of LCPF-LIG-25 as evidenced by the $R_{\rm s}$ results. The SCs also had good stability for repeated cycling and long-term storage. There was no drop of the capacitance over 500 cycles (Figure S12a). After 30-day storage under ambient conditions, the devices showed similar EDLC behavior as well as no capacitance drop (Figure S12b,c). This suggested that the device was stable enough against the acidic solid-state electrolyte over a long period with decent EDLC behavior retained.

The CV curves of SCs prepared on LCPF by 22% and 19% laser power levels are shown in Figure S12d,e. When lower laser power levels were used, the $C_{\rm A}$ increased from 0.57 to 1.52 mF/cm² at a scan rate of 0.01 V/s (Figure S12f), which is likely due to more graphene preserved on the substrates. Even though a higher laser power can ensure improved graphitization of the precursor, extra power may cause partial exfoliation of LIG from the film surface, leading to the loss of active sites for the formation of the electrical double layer.

Dopamine Sensor. The LCPF-LIG-25 was further used to fabricate on-chip dopamine sensors. The device was configured with LIG serving as both the working electrode and counter electrode and the Ag/AgCl electrode as the reference electrode, as shown in the inset in Figure 10a. It is worth mentioning that a complete on-chip sensor can be fabricated by preparing the LIG-based homemade reference electrode using Ag/AgCl ink, although such device fabrication was not explored here.⁶¹ The fabricated dopamine sensor required minimal sampling of dopamine solution. Figure 10a compares the CV curves at a scan rate of 50 mV/s with and without dopamine. No current peak was observed in the absence of dopamine, that is, PBS buffer only, while the prominent oxidation peaks appeared when 1 mM dopamine was used for testing. These results confirmed the dopamine detection ability of the LIG-embedded biomass-based films. With the scan rate increasing from 10 to 80 mV/s, the intensity of both anodic

and cathodic peaks increased accordingly (Figure 10b). The linear relationship between the intensity of these peaks and the square root of the scan rate suggested a diffusion-limited process (inset in Figure 10b). The DPV response was evaluated across varying dopamine concentrations (1×10^{-6} to 40×10^{-6} M) (Figure 10c). A positive linear correlation was observed between the intensity of the oxidant peak and dopamine concentration (Figure 10d). Compared to some other carbon-based electrodes, $^{62-64}$ the sensor showed great sensitivity ($2080~\mu A~mM^{-1}~cm^{-2}$). The limit of detection (LOD) was 0.659×10^{-6} M (S/N = 3), which was much lower than that of the previously reported biomass-derived dopamine sensor. 12

CONCLUSIONS

A green and facile technique was developed to convert lignocellulosic biomass into LIG-based electronics. The biomass-based films were fabricated from the cellulose pulps of corn stover pretreated by three DESs including ChCl:FA, ChCl:EG, and ChCl:OA. Differing from the other two DESs, pseudo-lignin formation occurred during ChCl:OA pretreatment. Direct laser writing was successfully applied to the fabricated films to form high-quality LIG. In addition to regenerated lignin, pseudo-lignin formed from side reactions of carbohydrate-based compounds was proven to be a good precursor for LIG formation. The findings provide new insights into lignin or aromatic biopolymer as a precursor for LIG production. Furthermore, the work suggests that porous graphene can be synthesized from carbohydrates involving controlled reactions of sugars into pseudo-lignin, humins, and so on. The LIG-embedded biomass-based films were well suited for the fabrication of on-chip disposable electronic devices including supercapacitors and dopamine sensors. The promising performance of the biomass-derived electronics suggests a new direction for converting biomass into graphenebased materials and devices.

■ ASSOCIATED CONTENT

Supporting Information

The Supporting Information is available free of charge at https://pubs.acs.org/doi/10.1021/acssuschemeng.2c02586.

Additional experimental section including calculation of crystallite size based on Raman data, preparation and DES pretreatment of bleached pulp, and preparation of pseudo-lignin from model compounds; possible reaction pathways for pseudo-lignin formation; and additional characterization data including optical photos, SEM images, TEM images, NMR spectrum, FTIR spectrum, tensile strength, contact angle, XPS survey spectra, Raman spectrum, and supercapacitor performance (PDF)

AUTHOR INFORMATION

Corresponding Author

Caixia Wan – Department of Biomedical, Biological, and Chemical Engineering, University of Missouri, Columbia 65211 Missouri, United States; orcid.org/0000-0001-5490-7490; Phone: +1 573 884 7882; Email: wanca@missouri.edu; Fax: +1 573 884 5650

Authors

- Hanwen Zhang Department of Biomedical, Biological, and Chemical Engineering, University of Missouri, Columbia 65211 Missouri, United States
- Yisheng Sun Department of Biomedical, Biological, and Chemical Engineering, University of Missouri, Columbia 65211 Missouri, United States
- Qianwei Li Department of Biomedical, Biological, and Chemical Engineering, University of Missouri, Columbia 65211 Missouri, United States

Complete contact information is available at: https://pubs.acs.org/10.1021/acssuschemeng.2c02586

Author Contributions

The manuscript was written through contributions of all the authors. The authors have given approval to the final version of the manuscript.

Notes

The authors declare no competing financial interest.

ACKNOWLEDGMENTS

This work was supported by the National Science Foundation (award no. 1933861) and USDA National Institute of Food and Agriculture (award no. 2021-67021-34504). The Authors thank Dr. Steven Kelley at the Chemistry Department in University of Missouri for the support for XRD analysis and Dr. Lingyu Chi at the Chemistry Department in Missouri University of Science and Technology for the support for NMR analysis.

REFERENCES

- (1) Su, D. S.; Perathoner, S.; Centi, G. Nanocarbons for the development of advanced catalysts. *Chem. Rev.* **2013**, *113*, 5782–
- (2) Nayak, P.; Kurra, N.; Xia, C.; Alshareef, H. N. Highly efficient laser scribed graphene electrodes for on-chip electrochemical sensing applications. *Adv. Electron. Mater.* **2016**, *2*, 1600185.
- (3) Li, D.; Sun, Y.; Chen, S.; Yao, J.; Zhang, Y.; Xia, Y.; Yang, D. Highly porous FeS/carbon fibers derived from Fe-carrageenan biomass: High-capacity and durable anodes for sodium-ion batteries. *ACS Appl. Mater. Interfaces* **2018**, *10*, 17175–17182.
- (4) Yoon, M.; Yang, S.; Hicke, C.; Wang, E.; Geohegan, D.; Zhang, Z. Calcium as the superior coating metal in functionalization of carbon fullerenes for high-capacity hydrogen storage. *Phys. Rev. Lett.* **2008**, *100*, No. 206806.
- (5) Harris, P. J. Carbon nanotube composites. *Int. Mater. Rev.* 2004, 49, 31–43.
- (6) Geim, A. K. Graphene: Status and prospects. Science 2009, 324, 1530–1534.
- (7) Liang, Y.; Chen, L.; Zhuang, D.; Liu, H.; Fu, R.; Zhang, M.; Wu, D.; Matyjaszewski, K. Fabrication and nanostructure control of superhierarchical carbon materials from heterogeneous bottlebrushes. *Chem. Sci.* **2017**, *8*, 2101–2106.
- (8) Lin, J.; Peng, Z.; Liu, Y.; Ruiz-Zepeda, F.; Ye, R.; Samuel, E. L.; Yacaman, M. J.; Yakobson, B. I.; Tour, J. M. Laser-induced porous graphene films from commercial polymers. *Nat. Commun.* **2014**, *5*, 5714.
- (9) Ye, R.; James, D. K.; Tour, J. M. Laser-induced graphene: From discovery to translation. *Adv. Mater.* **2019**, *31*, 1803621.
- (10) Zhang, W.; Lei, Y.; Ming, F.; Jiang, Q.; Costa, P. M. F. J.; Alshareef, H. N. Lignin laser lithography: A direct-write method for fabricating 3d graphene electrodes for microsupercapacitors. *Adv. Energy Mater.* **2018**, *8*, 1801840.

- (11) Mahmood, F.; Zhang, H.; Lin, J.; Wan, C. Laser-induced graphene derived from kraft lignin for flexible supercapacitors. ACS Omega 2020, 5, 14611–14618.
- (12) Mahmood, F.; Sun, Y.; Wan, C. Biomass-derived porous graphene for electrochemical sensing of dopamine. *RSC Adv.* **2021**, *11*, 15410–15415.
- (13) Kulyk, B.; Silva, B. F. R.; Carvalho, A. F.; Barbosa, P.; Girão, A. V.; Deuermeier, J.; Fernandes, A. J. S.; Figueiredo, F. M. L.; Fortunato, E.; Costa, F. M. Laser-induced graphene from paper by ultraviolet irradiation: Humidity and temperature sensors. *Adv. Mater. Technol.* **2022**, *7*, 2101311.
- (14) Chyan, Y.; Ye, R.; Li, Y.; Singh, S. P.; Arnusch, C. J.; Tour, J. M. Laser-induced graphene by multiple lasing: Toward electronics on cloth, paper, and food. *ACS Nano* **2018**, *12*, 2176–2183.
- (15) Zang, X.; Shen, C.; Chu, Y.; Li, B.; Wei, M.; Zhong, J.; Sanghadasa, M.; Lin, L. Laser-induced molybdenum carbide-graphene composites for 3d foldable paper electronics. *Adv. Mater.* **2018**, *30*, 1800062.
- (16) Kulyk, B.; Matos, M.; Silva, B. F. R.; Carvalho, A. F.; Fernandes, A. J. S.; Evtuguin, D. V.; Fortunato, E.; Costa, F. M. Conversion of paper and xylan into laser-induced graphene for environmentally friendly sensors. *Diamond Relat. Mater.* 2022, 123, No. 108855.
- (17) Ye, R.; Chyan, Y.; Zhang, J.; Li, Y.; Han, X.; Kittrell, C.; Tour, J. M. Laser-induced graphene formation on wood. *Adv. Mater.* **2017**, *29*, 1702211.
- (18) Carvalho, A. F.; Fernandes, A. J. S.; Martins, R.; Fortunato, E.; Costa, F. M. Laser-induced graphene piezoresistive sensors synthesized directly on cork insoles for gait analysis. *Adv. Mater. Technol.* **2020**, *5*, 2000630.
- (19) Xia, Q.; Chen, C.; Yao, Y.; Li, J.; He, S.; Zhou, Y.; Li, T.; Pan, X.; Yao, Y.; Hu, L. A strong, biodegradable and recyclable lignocellulosic bioplastic. *Nat. Sustain.* **2021**, *4*, 627–635.
- (20) Chen, M.; Zhang, X.; Liu, C.; Sun, R.; Lu, F. Approach to renewable lignocellulosic biomass film directly from bagasse. *ACS Sustainable Chem. Eng.* **2014**, *2*, 1164–1168.
- (21) Araújo, D.; Vilarinho, M.; Machado, A. Effect of combined dilute-alkaline and green pretreatments on corncob fractionation: Pretreated biomass characterization and regenerated cellulose film production. *Ind. Crops Prod.* **2019**, *141*, No. 111785.
- (22) Shikinaka, K.; Otsuka, Y.; Navarro, R. R.; Nakamura, M.; Shimokawa, T.; Nojiri, M.; Tanigawa, R.; Shigehara, K. Simple and practicable process for lignocellulosic biomass utilization. *Green Chem.* **2016**, *18*, 5962–5966.
- (23) Procentese, A.; Johnson, E.; Orr, V.; Garruto Campanile, A.; Wood, J. A.; Marzocchella, A.; Rehmann, L. Deep eutectic solvent pretreatment and subsequent saccharification of corncob. *Bioresour. Technol.* **2015**, *192*, 31–36.
- (24) Ji, Q.; Yu, X.; Yagoub, A. E.-G. A.; Chen, L.; Zhou, C. Efficient cleavage of strong hydrogen bonds in sugarcane bagasse by ternary acidic deep eutectic solvent and ultrasonication to facile fabrication of cellulose nanofibers. *Cellulose* **2021**, *28*, *6*159–6182.
- (25) Yu, Y.; Cheng, W.; Li, Y.; Wang, T.; Xia, Q.; Liu, Y.; Yu, H. Tailored one-pot lignocellulose fractionation to maximize biorefinery toward versatile xylochemicals and nanomaterials. *Green Chem.* **2022**, 24, 3257–3268.
- (26) Liu, Y.; Chen, W.; Xia, Q.; Guo, B.; Wang, Q.; Liu, S.; Liu, Y.; Li, J.; Yu, H. Efficient cleavage of lignin-carbohydrate complexes and ultrafast extraction of lignin oligomers from wood biomass by microwave-assisted treatment with deep eutectic solvent. *ChemSuschem* **2017**, *10*, 1692–1700.
- (27) Wan, G.; Zhang, Q.; Li, M.; Jia, Z.; Guo, C.; Luo, B.; Wang, S.; Min, D. How pseudo-lignin is generated during dilute sulfuric acid pretreatment. *J. Agric. Food Chem.* **2019**, *67*, 10116–10125.
- (28) Liu, X.; Xiao, W.; Ma, X.; Huang, L.; Ni, Y.; Chen, L.; Ouyang, X.; Li, J. Conductive regenerated cellulose film and its electronic devices a review. *Carbohydr. Polym.* **2020**, 250, No. 116969.
- (29) Nie, S.; Hao, N.; Zhang, K.; Xing, C.; Wang, S. Cellulose nanofibrils-based thermally conductive composites for flexible electronics: A mini review. *Cellulose* **2020**, *27*, 4173–4187.

- (30) Kulyk, B.; Silva, B. F. R.; Carvalho, A. F.; Silvestre, S.; Fernandes, A. J. S.; Martins, R.; Fortunato, E.; Costa, F. M. Laser-induced graphene from paper for mechanical sensing. *ACS Appl. Mater. Interfaces* **2021**, *13*, 10210–10221.
- (31) Zhang, T.; Zhang, X.; Chen, Y.; Duan, Y.; Zhang, J. Green fabrication of regenerated cellulose/graphene films with simultaneous improvement of strength and toughness by tailoring the nanofiber diameter. ACS Sustainable Chem. Eng. 2017, 6, 1271–1278.
- (32) Zhang, Y.; Hui, S.; Lin, X.; Ying, Z.; Li, Y.; Xie, J. Novel effective strategy for high-performance biomass-based super-flexible hierarchically porous carbon fibrous film electrode for supercapacitors. *J. Alloys Compd.* **2021**, 883, No. 160713.
- (33) Sluiter, A.; Hames, B.; Ruiz, R.; Scarlata, C.; Sluiter, J.; Templeton, D.; Crocker, D. L. A. P. Determination of structural carbohydrates and lignin in biomass. *Laboratory analytical procedure* **2008**, *1617*, 1–16.
- (34) Ben, H.; Ragauskas, A. J. Torrefaction of loblolly pine. *Green Chem.* 2012, 14, 72-76.
- (35) Shinde, S. D.; Meng, X.; Kumar, R.; Ragauskas, A. J. Recent advances in understanding the pseudo-lignin formation in a lignocellulosic biorefinery. *Green Chem.* **2018**, *20*, 2192–2205.
- (36) Hu, F.; Jung, S.; Ragauskas, A. Pseudo-lignin formation and its impact on enzymatic hydrolysis. *Bioresour. Technol.* **2012**, *117*, 7–12.
- (37) Sannigrahi, P.; Kim, D. H.; Jung, S.; Ragauskas, A. Pseudolignin and pretreatment chemistry. *Energy Environ. Sci.* **2011**, 4, 1306–1310.
- (38) Wikberg, H.; Liisamaunu, S. Characterisation of thermally modified hard- and softwoods by c cpmas nmr. *Carbohydr. Polym.* **2004**, *58*, 461–466.
- (39) Ma, X.; Yang, X.; Zheng, X.; Chen, L.; Huang, L.; Cao, S.; Akinosho, H. Toward a further understanding of hydrothermally pretreated holocellulose and isolated pseudo lignin. *Cellulose* **2015**, 22, 1687–1696.
- (40) Kumar, R.; Hu, F.; Sannigrahi, P.; Jung, S.; Ragauskas, A. J.; Wyman, C. E. Carbohydrate derived-pseudo-lignin can retard cellulose biological conversion. *Biotechnol. Bioeng.* **2013**, *110*, 737–753.
- (41) He, J.; Huang, C.; Lai, C.; Huang, C.; Li, M.; Pu, Y.; Ragauskas, A. J.; Yong, Q. The effect of lignin degradation products on the generation of pseudo-lignin during dilute acid pretreatment. *Ind. Crops Prod.* **2020**, *146*, No. 112205.
- (42) Garcia-Quiles, L.; Cuello, A. F.; Castell, P. Sustainable materials with enhanced mechanical properties based on industrial polyhydroxyalkanoates reinforced with organomodified sepiolite and montmorillonite. *Polymer* **2019**, *11*, 696.
- (43) Zhao, J.; Zhang, H.; Ma, C.; Han, H.; Sun, R.; Xie, M. Binary modification of eucommia ulmoides gum toward rlastomer with tunable mechanical properties and good compatibility. *J. Polym. Sci., Part A: Polym. Chem.* **2019**, *57*, 1247–1255.
- (44) Joelsson, T.; Pettersson, G.; Norgren, S.; Svedberg, A.; Höglund, H.; Engstrand, P. High strength paper from high yield pulps by means of hot-pressing. *Nord. Pulp Pap. Res. J.* **2020**, 35, 195–204.
- (45) Ferrari, A. C.; Meyer, J. C.; Scardaci, V.; Casiraghi, C.; Lazzeri, M.; Mauri, F.; Piscanec, S.; Jiang, D.; Novoselov, K. S.; Roth, S.; et al. Raman spectrum of graphene and graphene layers. *Phys. Rev. Lett.* **2006**, *97*, No. 187401.
- (46) Jorio, A.; Ferreira, E. H. M.; Moutinho, M. V. O.; Stavale, F.; Achete, C. A.; Capaz, R. B. Measuring disorder in graphene with the g and d bands. *Phys. Status Solidi* (b) **2010**, 247, 2980–2982.
- (47) Cançado, L. G.; Takai, K.; Enoki, T.; Endo, M.; Kim, Y. A.; Mizusaki, H.; Jorio, A.; Coelho, L. N.; Magalhães-Paniago, R.; Pimenta, M. A. General equation for the determination of the crystallite size la of nanographite by raman spectroscopy. *Appl. Phys. Lett.* **2006**, *88*, 163106.
- (48) Luong, D. X.; Yang, K.; Yoon, J.; Singh, S. P.; Wang, T.; Arnusch, C. J.; Tour, J. M. Laser-induced graphene composites as multifunctional surfaces. *ACS Nano* **2019**, *13*, 2579–2586.

- (49) Li, Z.; Zhai, H.; Zhang, Y.; Yu, L. Cell morphology and chemical characteristics of corn stover fractions. *Ind. Crops Prod.* **2012**, *37*, 130–136.
- (50) Kocaefe, D.; Huang, X.; Kocaefe, Y.; Boluk, Y. Quantitative characterization of chemical degradation of heat-treated wood surfaces during artificial weathering using xps. *Surf. Interface Anal.* **2013**, 45, 639–649.
- (51) Smith, M.; Scudiero, L.; Espinal, J.; McEwen, J.-S.; Garcia-Perez, M. Improving the deconvolution and interpretation of XPS spectra from chars by *ab* initio calculations. *Carbon* **2016**, *110*, 155–171
- (52) Barinov, A.; Gregoratti, L.; Dudin, P.; La Rosa, S.; Kiskinova, M. Imaging and spectroscopy of multiwalled carbon nanotubes during oxidation: Defects and oxygen bonding. *Adv. Mater.* **2009**, *21*, 1916–1920.
- (53) Ganesan, K.; Ghosh, S.; Gopala Krishna, N.; Ilango, S.; Kamruddin, M.; Tyagi, A. K. A comparative study on defect estimation using XPS and raman spectroscopy in few layer nanographitic structures. *Phys. Chem. Chem. Phys.* **2016**, *18*, 22160–22167.
- (54) Estrade-Szwarckopf, H. XPS photoemission in carbonaceous materials: A "defect" peak beside the graphitic asymmetric peak. *Carbon* **2004**, *42*, 1713–1721.
- (55) Zhu, Y.; Murali, S.; Stoller, M. D.; Ganesh, K. J.; Cai, W.; Ferreira, P. J.; Pirkle, A.; Wallace, R. M.; Cychosz, K. A.; Thommes, M.; et al. Carbon-based supercapacitors produced by activation of graphene. *Science* **2011**, 332, 1537–1541.
- (56) Radich, E. J.; Kamat, P. V. Making graphene holey. Gold-nanoparticle-mediated hydroxyl radical attack on reduced graphene oxide. *ACS Nano* **2013**, *7*, 5546–5557.
- (57) Uthaisar, C.; Barone, V. Edge effects on the characteristics of Li diffusion in graphene. *Nano Lett.* **2010**, *10*, 2838–2842.
- (58) Zhang, C.; Xie, Y.; Zhang, C.; Lin, J. Upgrading coal to multifunctional graphene-based materials by direct laser scribing. *Carbon* **2019**, *153*, 585–591.
- (59) Wei, D.; Wu, B.; Guo, Y.; Yu, G.; Liu, Y. Controllable chemical vapor deposition growth of few layer graphene for electronic devices. *Acc. Chem. Res.* **2013**, *46*, 106–115.
- (60) Peng, Z.; Ye, R.; Mann, J. A.; Zakhidov, D.; Li, Y.; Smalley, P. R.; Lin, J.; Tour, J. M. Flexible boron-doped laser-induced graphene microsupercapacitors. *ACS Nano* **2015**, *9*, 5868–5875.
- (61) Lei, Y.; Alshareef, A. H.; Zhao, W.; Inal, S. Laser-scribed graphene electrodes derived from lignin for biochemical sensing. ACS Appl. Nano Mater. 2019, 3, 1166–1174.
- (62) Dong, X.; Ma, Y.; Zhu, G.; Huang, Y.; Wang, J.; Chan-Park, M. B.; Wang, L.; Huang, W.; Chen, P. Synthesis of graphene—carbon nanotube hybrid foam and its use as a novel three-dimensional electrode for electrochemical sensing. *J. Mater. Chem.* **2012**, 22, 17044–17048.
- (63) Liu, J.; He, Z.; Xue, J.; Yang Tan, T. T. A metal-catalyst free, flexible and free-standing chitosan/vacuum-stripped graphene/polypyrrole three dimensional electrode interface for high performance dopamine sensing. *J. Mater. Chem. B* **2014**, *2*, 2478–2482.
- (64) Li, J.; Yang, J.; Yang, Z.; Li, Y.; Yu, S.; Xu, Q.; Hu, X. Graphene—Au nanoparticles nanocomposite film for selective electrochemical determination of dopamine. *Anal. Methods* **2012**, *4*, 1725—1728